A multiscale framework for simulating landslide runout and impact with barriers

A multiscale framework for simulating landslide runout and impact with barriers / Pasqua, A., Leonardi, A., Pirulli, M.. - In: CANADIAN GEOTECHNICAL JOURNAL. - ISSN 0008-3674. - STAMPA. - 62:(2025), pp. 1-19. [10.1139/cgj-2025-0034]

Publisher:
Canadian Science Publishing

Published
DOI:10.1139/cgj-2025-0034

Canadian Geotechnical Journal

OPEN ACCESS | Research Article

A multiscale framework for simulating landslide runout and impact with barriers

A. Pasqua[a], **A. Leonardi**[a], **and M. Pirulli**[b]

[a]School of Mechanical, Aerospace and Civil Engineering, The University of Sheffield, Western Bank, Sheffield S10 2TN, United Kingdom; [b]Department of Structural, Geotechnical and Building Engineering, Politecnico di Torino, Corso Duca degli Abruzzi, 24, Torino 10129, Italy

Corresponding author: **A. Pasqua** (email: a.pasqua@sheffield.ac.uk)

Abstract

This study proposes a multiscale framework for simulating landslide runout and its impact on mitigation structures, particularly focusing on debris flows. The proposed methodology combines depth-averaged (DA) models for basin-scale flow propagation with three-dimensional (3D) models for detailed impact analysis. This multiscale approach effectively balances computational efficiency with the need for detailed simulation in critical areas, such as the barrier near-field. Validation is conducted using both laboratory-scale experiments and a real-world case study in the Italian Alps. The results demonstrate the capability of the framework to accurately replicate flow dynamics, including run-up, velocity profiles, and flow lamination operated by barriers. To our knowledge, this represents the first validated application of a DA-3D multiscale framework for debris flow-barrier interactions at the site scale. The study also introduces a novel 3D adaptation of the widely used Voellmy rheology, which allows consistent cross-scale parameterisation. This framework enables simulating debris flows at the site scale with a precision previously confined to the laboratory scale.

Key words: granular flows, landslides, debris flows, depth-averaged method, 3D Lattice-Boltzmann method, hazard mitigation

Résumé

Cette étude propose un cadre multiscalaire pour simuler la propagation des glissements de terrain et leur impact sur les ouvrages de protection, en mettant particulièrement l'accent sur les coulées de débris. La méthodologie proposée combine des modèles moyennés en profondeur (DA) pour la propagation des écoulements à l'échelle du bassin avec des modèles tridimensionnels (3D) pour une analyse détaillée des impacts. Cette approche multiscalaire équilibre efficacement l'efficacité computationnelle avec le besoin de simulations détaillées dans les zones critiques, comme le champ proche des barrières. La validation est effectuée à l'aide d'expériences en laboratoire à petite échelle et d'une étude de cas réelle dans les Alpes italiennes. Les résultats démontrent la capacité du cadre à reproduire avec précision la dynamique de l'écoulement, y compris la remontée, les profils de vitesse et la stratification du flux induite par les barrières. À notre connaissance, il s'agit de la première application validée d'un cadre multiscalaire DA-3D pour les interactions entre coulées de débris et barrières à l'échelle du site. L'étude présente également une nouvelle adaptation 3D de la rhéologie de Voellmy, largement utilisée, permettant une paramétrisation cohérente entre les différentes échelles. Ce cadre permet de simuler les coulées de débris à l'échelle du site avec une précision auparavant limitée à l'échelle du laboratoire.

Mots-clés : ecoulements granulaires, glissements de terrain, coulées de débris, méthode moyennée en profondeur, méthode 3D de Lattice-Boltzmann, atténuation des risques

Introduction

Debris flows consist of a mixture of water, mud, and poorly-sorted debris of various sizes that flow under the influence of gravity in natural channels (Takahashi 1981; Iverson 1997). Due to the high speed and lack of warning signs, they often lead to casualties (Larsen et al. 2001; García-Delgado et al. 2019), as well as catastrophic economic damage (Winter et al. 2016). As a consequence, mitigation structures such as barriers are frequently installed on the flow paths. Figure 1 illustrates various types of barriers. Their purpose is to dissipate energy (Ashwood and Hungr 2016), laminate the flow (Leonardi et al. 2016), and retain the largest boulders (Zhao et al. 2020). Standardised design procedures, like those provided by the Austrian guidelines (Hübl et al. 2017) are based on simplified pressure profiles at impact, i.e., hydrodynamic, hydrostatic, or a combination of both. These guidelines provide important design principles, but they often overlook the three-dimensional and unsteady nature of debris flows,

Fig. 1. Examples of typical barriers installed in areas prone to debris flows: (*a*) slit dam, (*b*, *c*) filter barriers, and (*d*) cable-net barrier.

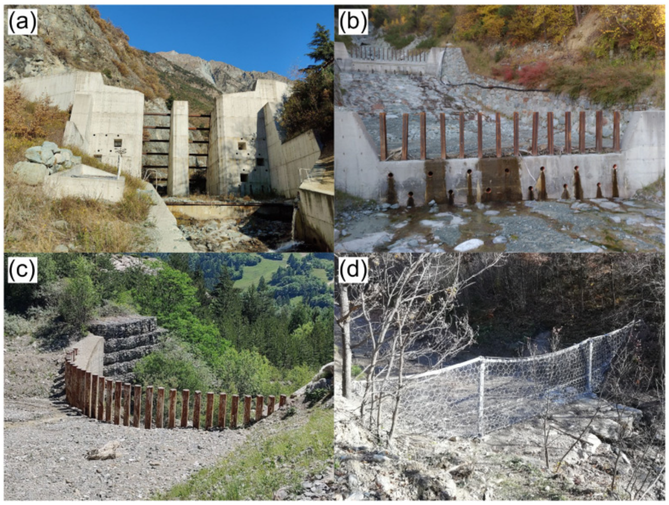

which lead to stress concentrations in various areas of the barrier (Leonardi et al. 2019) and which may not adhere strictly to the prescribed hydrodynamic or hydrostatic principles. Thus, relying solely on an analytical model for designing mitigation structures may not lead to a fully optimised design. This motivates the need for simulation frameworks that resolve the full physics of debris flow interaction with structures while remaining computationally feasible at real-world scales.

To complement guideline-based approaches, the scientific community has developed physical and numerical models. Physical modelling can be carried out at large-scale facilities or at the laboratory scale, each presenting unique challenges. Large-scale modelling requires ample space and significant investments for construction. On the other hand, laboratory-scale modelling faces scaling issues (Iverson et al. 2010; Iverson 2015).

On the other hand, numerical models are not directly influenced by scale effects, require fewer economic resources, and allow for repeatable simulations without material availability constraints. They usually fall within either discrete- or continuum-based models. Discrete models approximate the flow by representing it as a collection of discrete elements (Marchelli et al. 2020). Particle velocity and trajectory are calculated at each time step, and various properties, including pressure and forces, are linked to the kinetic energy of the particles. Notwithstanding the advantages of this approach, the computational demands of simulating numerous elements pose a challenge (Furuichi and Nishiura 2017). Continuum-based numerical approaches represent a valid alternative. They simplify the composition to an equivalent continuum medium, whose characteristics stem from the constituent particles and fluids.

A large variety of continuum models have been proposed in both depth-averaged (DA) and three-dimensional (3D) forms. DA was first proposed by Savage and Hutter (1989) for debris flows. The authors depth-averaged the mass and momentum conservation equations and considered the resistance to flowing to be localised at the interface between flow and topography. The method was later modified and improved and is nowadays mature (Pudasaini and Mergili 2024). However, it retains limitations in studying impact against mitigation structures, such as those developing with mitigation barriers. The depth-averaging process results in the loss of information on momentum transfer along the flow depth, potentially oversimplifying impact representation. For this reason, 3D models are growingly employed to study impact, as they can calculate internal shear deformation and all velocity components across the flow depth.

In this respect, 3D FEM-based models have been proposed. For example, Kumar et al. (2019) studied the stability of slopes prone to generating landslides. Lagrangian FEM-based models may be inaccurate in case of large deformations due to mesh distortion, and PFEM models were developed to address this issue by employing frequent remeshing and low-order triangular elements (Yuan et al. 2019). Smooth particle hydrodynamics (SPH) and the material point method (MPM) are other alternatives. The former is a meshless method that is used to study large deformation problems (Peng et al. 2015; Chen et al. 2019). The latter is a mesh-based Eulerian–Lagrangian scheme that has been employed to study propagation and impact (Llano-Serna et al. 2016; Cuomo et al. 2021). Finally, an alternative is represented by the Lattice Boltzmann method (LBM). This is a 3D fluid solver capable of studying non-Newtonian fluids and impact. Its success is due to its high performance in parallel computing architectures (Habich et al. 2013; Obrecht et al. 2013), especially when managing challenging boundary conditions (Zhang 2011).

Regardless of the chosen solver, conducting a comprehensive 3D analysis of an entire debris-flow event at the site scale remains exceedingly time-consuming and complex. Moreover, having 3D resolution is not always justified in the propagation subdomain, i.e., where the flow is not influenced by barriers or complex topographical features. In this domain, a fully-3D simulation would not add important details compared to the same simulation performed with DA.

It follows that DA and 3D models are complementary in studying different aspects of debris flows. DA models are effective for analysing the propagation domain, while 3D models are better suited for studying impact. Notwithstanding, little attention has been paid to combining different numerical models to study impact as a function of upstream propagation. A multiscale framework that employs both 3D and DA model to study debris flows at the site scale has not yet been proposed, and this paper aims to fill this gap. To do this, this paper proposes an approach based on a domain decomposition, using a DA model and a 3D model on separate and combined, subdomains.

The literature offers some examples of similar strategies used in other contexts. For example, van Thang et al. (2010) studied a 1D problem using LBM to couple with various hydraulic interconnection structures to build models of complex irrigation networks. Domnik et al. (2013) coupled a DA model and a 2D model to study granular flows, and Pasqua

Fig. 2. Grand Valley basin, Saint Vincent, Italy. Topographical description of the basin with installed mitigation structures. The blue-shaded area represents the basin, while the green-shaded area highlights the municipality of Saint Vincent, which is prone to debris flows. Map projection: UTM-ED50. The base map is provided by "Servizi Cartografici SCT" of the Autonomous Region of Aosta Valley (Italy) (D'Aosta 2019). Modified after Leonardi and Pirulli (2020).

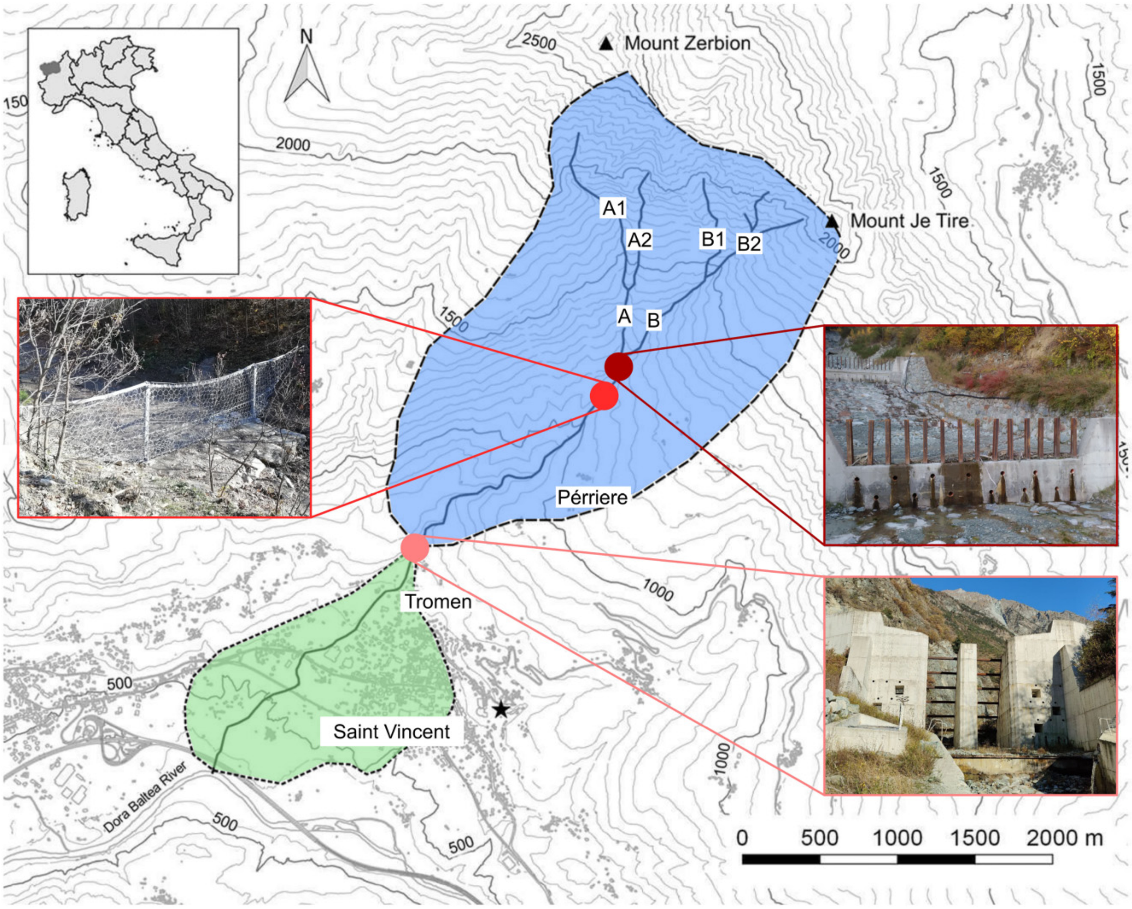

et al. (2022) coupled a 3D model and a DA model to back-analyse flow of sand in a laboratory chute. However, Pasqua et al. (2022) employed the μ(I) rheology, which is widely used at the laboratory scale but difficult to implement at the site scale due to its underlying assumptions. This paper builds on these earlier works, aiming at the full representation of prototype events at the site scale and supporting both the academic development of multiscale methods and their potential transfer to engineering practice in hazard-prone contexts.

Benchmark event and domain decomposition

The goal of this paper is the simulation of debris flows at the site scale, using a multiscale framework based on the DA-3D combining. The focus is on a benchmark event that occurred in 2016 in Saint Vincent, Italy. Figure 2 shows the geographical area of the event site and shows some of the mitigation structures present on site. It is situated in the Grand Valley basin, which covers an area of 5.22 km^2. The elevation of the basin ranges from 700 to 2719 m a.s.l., with average slopes of 12%–38%. The basin contains two main channels, labelled A and B in Fig. 2 composed of fractured rocks and materials such as schist and serpentinite. Channels A and B originate from the convergence of smaller channels: A1 and A2 forming channel A, and B1 and B2 forming channel B. These slopes, which have partial vegetation cover, are highly susceptible to rapid erosion during heavy or moderate rainfall events, which frequently occur in spring and summer. Additionally, the channels experience erosion during the summer due to the snowmelt. The combination of these factors makes debris flows a yearly-based recurring phenomenon.

Local authorities have installed various mitigation structures to address the risk associated with debris flows. Figure 2 reports some examples of installed mitigation structures. One of these structures is the filter barrier located at the confluence of channels A and B, as shown in Fig. 2. The barrier consists of a 1.0 mm high concrete base, spanning the entire width of the channel, with I-steel beams (IPE 270) embedded in the concrete base. Each beam is 2.7 m in height, spaced 0.6 m apart, and extends 2 m above the concrete base, resulting in an overall height of 3 m. This study focuses on this particular barrier due to the presence of a monitoring system,

Fig. 3. Application of the multiscale DA-3D combining framework to the Saint Vincent case study: (*a*) Overview of the basin modelled at a large scale using the DA model, with the blue-shaded area indicating the portion of the domain solved by the DA model. (*b*) Detailed view of the area surrounding the filter barrier, showing the flow direction, the domain studied by the 3D model, and the location of the interface section. (*c*) Example of the unstructured mesh used in the DA model. (*d*) Example of the mesh used in the 3D model (embedded within the DA model) and the interface section. (*e*) The mitigation structure analysed in this study using the multiscale framework. (*f*) Example of a barrier destroyed by a debris flow. Modified after Leonardi and Pirulli (2020).

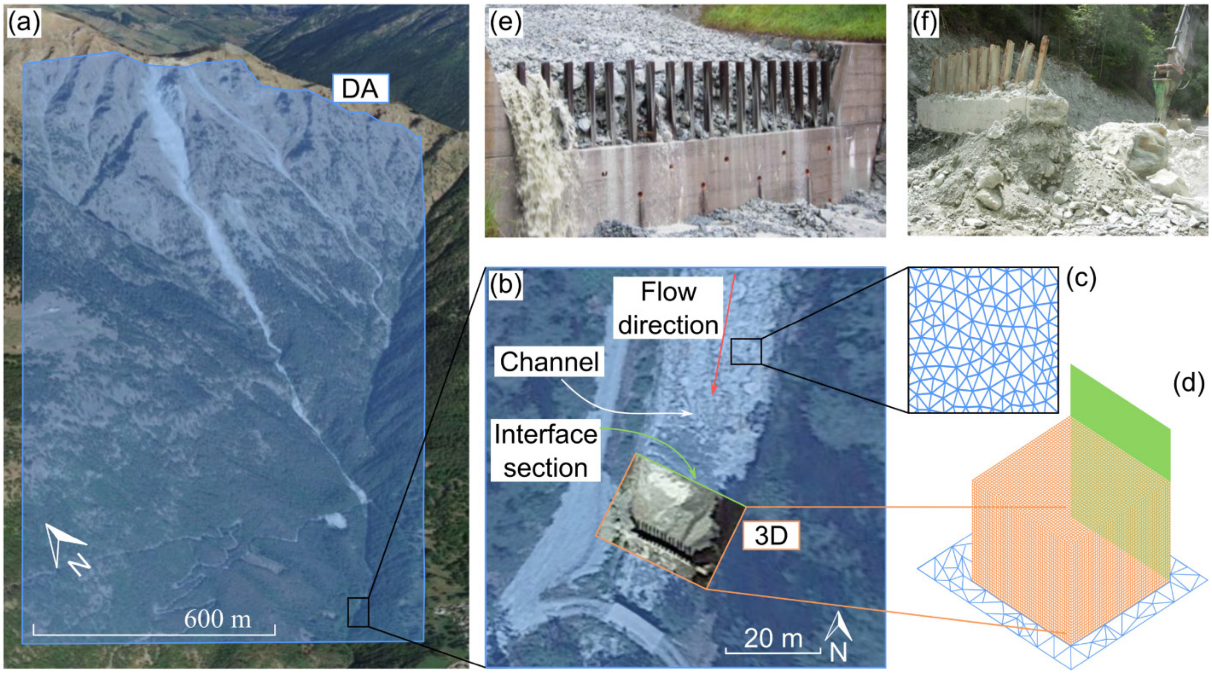

facilitating comparison with numerical results—a crucial aspect given the difficulty of obtaining field data on impacts. The monitoring system consists of strain gauges that measure the deformations of the beams caused by impact, allowing for the estimation of the forces acting on the beams. A complete description of the monitoring system is provided by Leonardi and Pirulli (2020).

As mentioned in the Introduction, 3D models are superior to DA for the simulation of impact. However, they are computationally demanding. To unlock the possibility of simulating impact without excessively simplifying the domain, the topography under study is divided into two numerical subdomains, as shown in Fig. 3. The DA model operates on a subdomain that includes the vast majority of the physical space. This includes the area where the flow propagation takes place. This subdomain is discretised on a planar projection using a 2D unstructured triangular mesh (see Figs. 3*a*–3*b*). On the area where the flow approaches a mitigation structure, shown in Fig. 3*d*, a second subdomain is defined. This is discretised using a much finer regular mesh, fully 3D, and capable to resolve impact. At the interface between the two subdomains, a interface section acts as interface between the 3D and the DA models, as shown in Fig. 3*c*.

Notably, the DA subdomain, Fig. 3*c*, can operate on a relatively coarse mesh, with spacing of the order of magnitude of meters. Such a mesh can accurately replicate the flow while maintaining a modest computational demand. In contrast, the 3D subdomain, being smaller, can employ a finer mesh, which can easily be of element size 10^{-2} m or less as shown in Fig. 3*d*. The specifics of the two meshes further highlight the advantages of this multiscale framework: the number of points is drastically reduced compared to a brute-force 3D approach. Furthermore, a multiscale approach may be a valuable tool for studying complex impact, such as those illustrated in Figs. 3*e*–3*f*, where barriers can be compromised by flows if not properly designed or if their design relies on oversimplified methods.

Simulation methods and combining

An overview of the solvers for the two subdomains, of the combining procedure, and of the unified description of the rheology is provided in the following.

DA subdomain

For the benchmarks presented in this paper, the DA subdomain is solved with the in-house finite-volume software RASH (Pirulli 2005). A complete description of this DA model is beyond the scope of this paper. Interested readers are directed to Mangeney-Castelnau (2003) or Pirulli (2010), and only an outline is provided here.

Fig. 4. Lattice structure in 3D LBM. (*a*) Representation of the regular spatial discretisation within the lattice. (*b*) The 19 discrete velocity vectors in the D3Q19 lattice configuration.

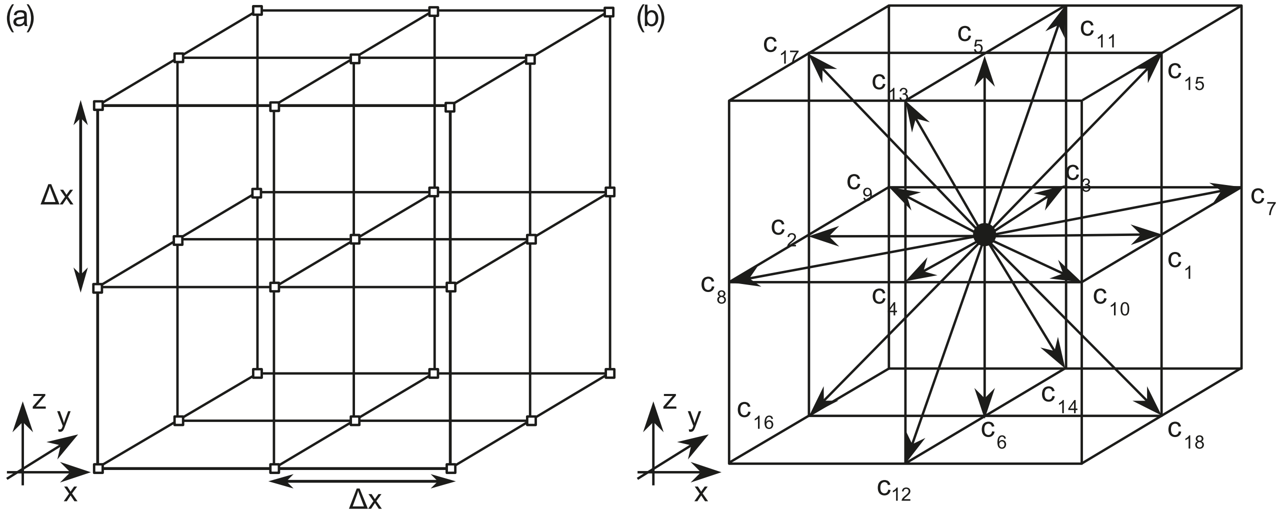

In the DA model, the flow is described as a single phase, incompressible, continuum medium with constant density. The depth-averaged velocity $\left(\bar{u}_x, \bar{u}_y\right)$ can be defined under the hypothesis that the flow depth h is much smaller than the flow length L. Thus, the equations that describe the evolving flow are the depth-averaged mass and momentum conservation. These can be written in a local reference frame as

$$\frac{\partial h}{\partial t} + \frac{\partial}{\partial x}\left(h\bar{u}_x\right) + \frac{\partial}{\partial y}\left(h\bar{u}_y\right) = 0 \tag{1}$$

$$\frac{\partial}{\partial t}\left(h\bar{u}_x\right) + \frac{\partial}{\partial x}\left(h\bar{u}_x^2\right) + \frac{\partial}{\partial y}\left(h\bar{u}_x\bar{u}_y\right) = g_x h + \frac{\partial}{\partial x}\left(g_z h^2/2\right) - \tau_{b,x} \tag{2}$$

$$\frac{\partial}{\partial t}\left(h\bar{u}_y\right) + \frac{\partial}{\partial x}\left(h\bar{u}_x\bar{u}_y\right) + \frac{\partial}{\partial y}\left(h\bar{u}_y^2\right) = g_y h + \frac{\partial}{\partial y}\left(g_z h^2/2\right) - \tau_{b,y} \tag{3}$$

where g is the gravity, and $\tau_{b,\,x}$ and $\tau_{b,\,y}$ express the shear resistance to flow, which can be prescribed based on the chosen rheological law.

3D subdomain

The impact subdomain is here solved using a 3D Lattice-Boltzmann method (LBM). The specific solver is the one originally developed by Leonardi et al. (2014) and further enhanced by Pasqua et al. (2022). However, the multiscale framework can be seen as solver-agnostic: it can potentially be assembled using other 3D solvers.

In LBM, the flow is described as a continuum through a density distribution function $f\left(\boldsymbol{x}, t, \boldsymbol{c}\right)$, defined as the probability of finding a fluid particle in the position $\boldsymbol{x}$ at time t, moving with speed $\boldsymbol{c}$. LBM drastically reduces the degrees of freedom by discretising the velocity space using a subset of allowed velocities c_i. These velocities stream mass from a point to another on a regular lattice with spacing Δx. In this paper, the popular D3Q19 lattice (3 dimensions and 19 velocities) is employed, as shown in Fig. 4.

LBM reconstructs density and velocity fields from straightforward summation of f_i. This is based on momentum and mass conservation:

$$\rho = \sum_i f_i \tag{4}$$

$$u = \sum_i f_i c_i/\rho \tag{5}$$

$$p = c_s^2 \rho \tag{6}$$

where ρ, u, and p are the fluid density, velocity, and pressure, respectively, and $c_s = \Delta x/\sqrt{3}\Delta t$ is the lattice speed of sound (Mohamad 2011). The evolution of f_i over a time step Δt follows the discretised Boltzmann equation

$$f_i\left(x + c_i\Delta x, t + \Delta t\right) = f_i\left(x, t\right) + \Delta t\Omega_i\left(x, t\right) \tag{7}$$

where Ω_i represents the collision operator. This can be approximated using the linear form proposed by Bhatnagar et al. (1954):

$$\Omega_i = \frac{f_i^{\mathrm{eq}} - f_i}{t_r} \tag{8}$$

In this form, t_r is a time, governing relaxation of the system towards thermodynamic equilibrium f_i^{eq}. Further details on the form of the f_i^{eq} are given by Zou and He (1997).

To simulate debris flow with LBM, the free surface position is tracked using the method proposed by Körner et al. (2006). In order to simulate non-Newtonian behaviour, the viscosity is directly related to t_r:

$$\nu\left(x, t\right) = \frac{t_r\left(x, t\right) - 1/2}{3}\frac{\Delta x^2}{\Delta t} \tag{9}$$

therefore treating t_r as a field variable. This approach has limitations: LBM demonstrates stability only within specified values of t_r, typically $\in [0.5005, 1.0]$. Therefore, in LBM, careful selection of Δx and Δt is crucial to scale down the desired viscosity range to compatible values of the relaxation time t_r. For frictional rheologies, the viscosity often diverges at the free surface, leading to instabilities. To deal with this issue, the regularisation proposed by Franci and Cremonesi (2019) is employed.

DA-3D combining

The DA and 3D models are employed sequentially. First, the DA model solves the entire domain, providing the flow depth and depth-averaged velocity at every location and time step. However, the two models operate with different time steps and spatial discretisation. The different time discretisations is handled with an interpolation procedure applied to the DA results, filling the temporal gap between two time steps of the 3D model. As a result, the DA model outputs are temporally aligned with the time resolution of the 3D model. From a spatial perspective, the former uses an unstructured triangular Delaunay mesh, while the latter employs a regular squared mesh with a finer time resolution. To ensure compatibility between the two models, spatial interpolation is performed, aligning the results of the DA model with the 3D mesh. Once the DA results are transferred onto the 3D mesh, the depth-averaged velocity is used to reconstruct the full 3D velocity profile. This transformation occurs at a defined interface section, where the DA and 3D subdomains are combined. The details of the spatial interpolation are described with more detail in Pasqua et al. (2022). The 3D and the DA subdomains are coupled at a user-defined section. There, a full 3D velocity profile is reconstructed from DA variables, $\bar{u}$ and h. The velocity profile is rheology specific, and is unique at steady state. This procedure has been tested by Pasqua et al. (2022) at the laboratory scale using the μ(I) rheology and its corresponding steady-state velocity profile. To extend the same principles to the site scale, a combining based on the widely employed Voellmy rheology (Pirulli 2010) is explored here instead.

In a DA framework, the Voellmy rheology is based on two parameters: the friction coefficient μ and a lump term for velocity-dependant dissipation ξ, which is generally referred to in the literature as the turbulence coefficient (Pirulli 2010). The basal resistance to flow τ_b is therefore written as

$$\tau_\mathrm{b} = \rho g h \mu + \rho g \frac{\bar{u}^2}{\xi} \tag{10}$$

ξ is an empirical coefficient that must be calibrated for each analysis.

The Voellmy rheology is not directly applicable to a 3D domain. This is because (i) the ξ term has no obvious local definition in 3D and (ii) values of ξ are often calibrated through back-analysis at the site scale and are scale-dependent.

To overcome this, a 3D expression of the Voellmy rheology is here proposed:

$$\tau\,(z) = \rho g h \mu + \rho l^{*2} \dot{\gamma}^2 \tag{11}$$

This defines the local shear resistance τ by combining friction and a velocity-dependent, Bagnold-like, dissipative term, written as a function of $\dot{\gamma} = \partial u / \partial z$, the second invariant of the shear rate tensor. In the Bagnold rheology, l^* is a reference particle diameter (Bagnold 1954). Here, it is instead interpreted as a reference length-scale for velocity-dependent dissipations to account for multiple sources of energy losses. It is analogous to ξ, and in principle, it should also be calibrated through back-analysis.

A clear advantage of this 3D formulation is that it leads to a velocity profile in stationary conditions. Assuming (i) an infinite slope with constant incline θ, (ii) friction localised at the base layer, (iii) a hydrostatic distribution of normal stresses, and (iv) that the shear resistance (eq. 11) is everywhere in equilibrium with the driving forces, the shear rate can be written as

$$\frac{\partial u}{\partial z} = \sqrt{\frac{(\tan\theta - \mu)\, g h \left(1 - \frac{z}{h}\right)\cos\theta}{l^{*2}}} \tag{12}$$

Integration leads to the following velocity profile:

$$u\,(z) = \frac{2}{3}\frac{h^{\frac{3}{2}}}{l^*}\sqrt{g\cos\theta\,(\tan\theta - \mu)}\left[1 - \left(1 - \frac{z}{h}\right)^{\frac{3}{2}}\right] \tag{13}$$

where a condition $\tan\theta > \mu$ determines whether the material flows.

The depth-averaged velocity at steady state in the Voellmy model can be derived by depth-averaging eq. 13:

$$\bar{u} = \frac{2}{5}\frac{h^{\frac{3}{2}}}{l^*}\sqrt{g\cos\theta\,(\tan\theta - \mu)} \tag{14}$$

By expressing the 3D velocity profile in terms of the DA velocity profile, one obtains

$$u\,(z) = \frac{5}{3}\bar{u}\left[1 - \left(1 - \frac{z}{h}\right)^{\frac{3}{2}}\right] \tag{15}$$

which directly extrapolates a velocity profile from the DA variables $\bar{u}$ and h. This can then be used as a template for the combining algorithm at the interface between 3D and DA models.

To keep the rheology unified across the scales, the rheological parameters must be consistent between the two subdomains. To do this, μ is assumed to be the same, while l^* is related to ξ. This is done by combining eqs. 10 and 14 and rearranging the terms to isolate l^*:

$$l^* = \frac{2}{5}h\sqrt{\frac{g}{\xi}} \tag{16}$$

It is crucial to note that l^* is expressed as a function of the flow height h. Given that l^* is interpreted as a material parameter, which remains constant throughout the simulation, a characteristic flow depth h^* needs to be selected.

The placement of the interface section is crucial for ensuring the accuracy and reliability of the combined model, given its current limitation of transferring information solely from the DA to the 3D model, without feedback in the opposite direction. This restriction implies that the flow must be supercritical, and as a result, the interface section must be positioned sufficiently far from regions where reflected waves, bores, or dead zones may form near mitigation structures (Faug 2015). A practical criterion for selecting the interface location is to ensure that the Froude number is high, as this confirms the flow is in a supercritical regime. Additionally, the interface should be placed where the vertical velocity component is negligible or close to zero (Domnik et al. 2013), as the DA model does not account for the vertical component of the velocity. By satisfying this condition, the transition between the DA and 3D models avoids introducing significant

Fig. 5. (*a*) Laboratory setup, with the storage tank located at the top of the flume and the double gate system highlighted in yellow. The camera-recorded area is highlighted in purple. (*b*) Scheme of the laboratory setup (not to scale). Due to the symmetry of the problem, a plane of symmetry is applied, and only half of the domain is modelled. (*c*) Glass beads used in the experiment. (*d*) Photograph of the glass beads flowing through the flume. (*e*) Planar view of the numerical setup, with the recorded area highlighted in purple. (*f*) Application of the multiscale DA-3D combining framework to the laboratory setup (planar view). The blue-shaded area represents the portion of the domain solved by the DA model, while the orange-shaded area is studied by the 3D model; the interface section is shown in green. The interface section position x_i is highlighted in green, and its position can be adjusted.

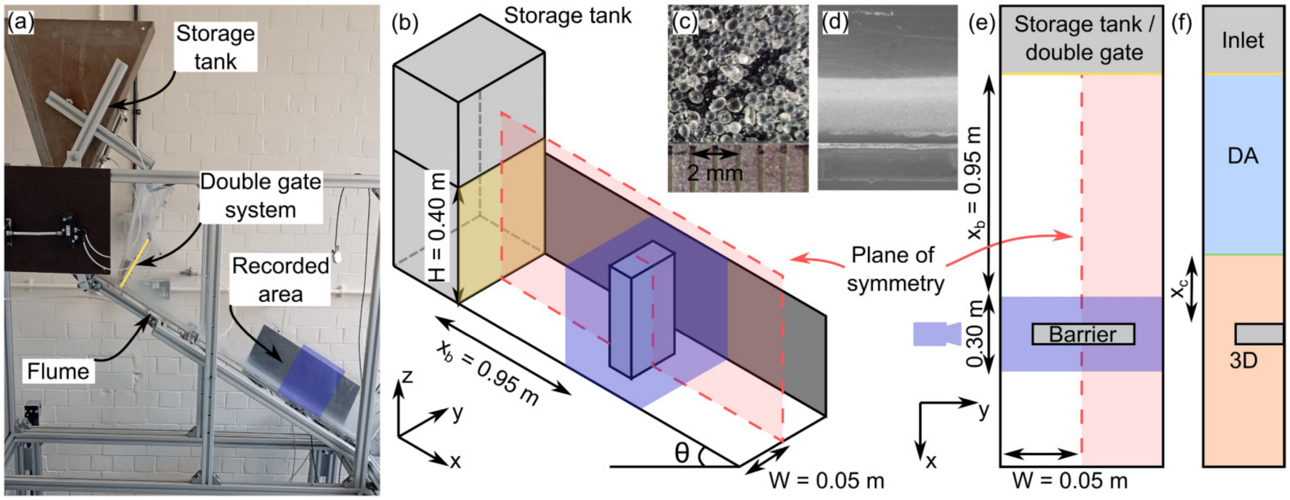

errors due to the absence of vertical velocity considerations in the DA formulation. If these conditions are met, the interface section can be placed arbitrarily close to the barrier, prioritizing efficiency.

Laboratory scale

In the proposed framework, the extent of the subdomains, and therefore the location of the interface section, is a function of the criteria discussed in Section DA-3D combining. From a computational perspective, it is advantageous to reduce the 3D subdomain as much as possible. However, if the interface section is too close to the barrier, accuracy might reduce. As it is difficult to address this issue at the field scale, this section firstly explores an application at the lab scale. This analysis doubles as validation.

Setup of physical and numerical models

To validate the multiscale framework, laboratory experiments conducted at the University of Sheffield are reported. The setup, depicted in Fig. 5, includes a flume with adjustable inclination and plexiglass walls. It is 1.20 m long and $W = 0.10$ m wide. Following Wu et al. (2022), the flume can be interpreted as a representation of a natural channel, featuring a mitigation structure. This is a rigid obstacle that extends partially across the flume width, situated $x_\mathrm{b} = 0.95$ m downstream from the release gate. The obstacle spans 50% of the flume width. As shown in Fig. 5*e*, only half of the prototype barrier is numerically modelled, with one of the smooth perspex wall representing a symmetry condition.

The experiments utilise 15 kg of glass beads with mean diameter 0.53 mm and density of 2470 kg/m^3, shown in Figs. 5*c*–5*d*. Variations of this material are widely employed in the literature, e.g., by Jop et al. (2006) and Barker and Gray (2017). The glass beads storage system is a tank with a double gate system, which produces a steady inflow by setting the inflow height. To prevent basal slip conditions, a layer of glass beads is glued to the flume base (Pouliquen 1999).

The flume slope is adjusted to produce realisations of impact for quasi-steady supercritical flows. At impact, the flows produce vertical jets, which are particularly challenging to simulate with DA models. Two calibration experiments are reported, at $\theta = 28^\circ$ and 30°, and with gate opening set to $H = 40$ mm. To capture the flow evolution, including flow depth and discharge, the experiments were recorded using a high-speed camera with a frame rate of 700 FPS and a resolution of 1280 × 1080 pixels, covering a 30 cm × 12 cm window. The flow discharge is recorded with another camera at 60 FPS, providing a measure of the mean volumetric flow rate Q. From this, the mean depth-averaged velocity at the gate inlet is estimated as $\bar{u}^* = Q/(HW)$.

Table 1 presents the results for the free-flow configurations. The flow depth and velocity data from this table are used to define the reference length scale h^* and velocity scale $\bar{u}^*$ for the studied case. From these, the reference time scale of the problem can be determined as $t^* = h^*/\bar{u}^*$. The free-flow tests are used to calibrate the rheology. Since the here investigated laboratory granular flow is dry and monodisperse, the μ(I) rheology is considered more appropriate. Unlike the Voellmy rheology, μ(I) has a robust theoretical framework that covers both DA and 3D (Pasqua et al. 2022) frameworks.

Table 1. Hydraulic values of the flows with no obstacle.

		28°	30°
Q	$\mathrm{m^3/s}$	$7.8 \cdot 10^{-4}$	$8.9 \cdot 10^{-4}$
h^*	m	0.015	0.012
$\bar{u}^*$	m/s	0.540	0.743
t^*	s	0.016	0.010
Fr	–	1.4	2.2

It is based on the hypothesis that the friction coefficient μ can be expressed as a function of the inertial number I:

$$\mathrm{I} = \frac{d\dot{\gamma}}{\sqrt{p/\rho_\mathrm{p}}} \tag{17}$$

where d and ρ_p are the particle diameter and the particle density respectively. The definition of I stems from the observation that a steady-state flow is achieved on an incline when the tangent of the slope angle $\tan\theta$ falls within two critical values: $\mu_\mathrm{s} = \tan\theta_\mathrm{s}$ and $\mu_\mathrm{d} = \tan\theta_\mathrm{d}$, representing the static and secondary friction coefficients, respectively (Pouliquen 1999).

The μ(I) rheology has established formulations in both 3D and DA form (Pouliquen 1999; Forterre and Pouliquen 2002). In the latter, the Inertial number is substituted with the Froude number:

$$\mu\,(\mathrm{Fr}) = \mu_\mathrm{s} + \frac{\mu_\mathrm{d} - \mu_\mathrm{s}}{\frac{\beta h}{L^* d \mathrm{Fr}} + 1} \tag{18}$$

In 3D, the familiar Inertial number controls friction:

$$\mu\,(\mathrm{I}) = \mu_\mathrm{s} + \frac{\mu_\mathrm{d} - \mu_\mathrm{s}}{\frac{\mathrm{I_0}}{\mathrm{I}} + 1} \tag{19}$$

In the formulations, I_0, β, and L^* are the other rheological parameters. A key advantage is that there is an established routine for converting parameters of the 3D formulation to equivalent DA ones, and vice-versa (Gray and Edwards 2014).

Focusing on the 3D formulation, Table 2 shows the typical values employed in the literature for glass beads. The table shows a large scatter, especially of μ_d and I_0, making it difficult to rely on the literature for calibration. Thus, we use the free-flow test for this purpose.

In 3D, three parameters need calibration: I_0, μ_s, and μ_d. We fix μ_s to 0.342, the value chosen by Barker and Gray (2017) for a very similar material. The two free-flow laboratory experiments (28° and 30°) are used to calibrate the remaining parameters. This is done by recording the steady-state values of h and $\bar{u}$, and inverting the expression of the depth-average velocity at steady state:

$$\bar{u} = \frac{2}{5} I_\theta \frac{1}{d} \sqrt{g \cos\theta h^3} \tag{20}$$

where I_θ is the inverse of the μ(I) function (Lagrée et al. 2011).

To verify the correctness of the implementation in the 3D and DA models, simpler infinite-slope realisations of flow are performed. For the standalone DA model, a mesh with spacing 2 mm is used, while the standalone 3D model employs a finer mesh with spacing $\Delta x = 0.8$ mm and a fixed time step of $\Delta t = 1 \times 10^{-5}$ s. These values ensure a sufficiently fine discretisation of the flow. In the 3D model, they also ensure that the model is able to simulate accurately the required viscosity range (Pasqua et al. 2022). Through these, it is confirmed that the experimental discharge conditions (Table 1) and the rheological values in Table 3 result in values of flow depth h and velocity $\bar{u}$ that match the measurements. These values are assumed stationary, and are used to scale all results as h^* and $\bar{u}^*$. A visualisation of these tests is provided in Fig. 6.

Results

Once the inlet discharge and rheological parameters are calibrated, the multiscale framework is applied to back-analyse the flume experiments in presence of the barrier. The decomposition of the subdomains is illustrated in Fig. 5*f*, and is variable with respect to the location of the interface section x_i, measured upstream from the barrier.

Figure 7 presents the experimental and numerical comparisons for both realisations (28° and 30°). In the figure, and everywhere thereafter, time after impact $t - t_0$ is scaled using the reference time scale of flow $t^* = h^*/\bar{u}^*$. The figure presents results with a 3D subdomain that extends up to 0.30 m/h^* upstream from the barrier. This is also the location of the interface section x_i. The repercussions of this choice are discussed later on.

In the numerical simulations, the visualisation is produced with a perfect orthogonal projection as the side view. However, in the laboratory, the camera records a prospective view, which also shows the flow surface across the flume width. To address this, a dashed black line was added to Fig. 7, indicating which surfaces are being compared: the flow height at the side perspex.

Both sets of results show remarkable agreement between the numerical and experimental outcomes. Impact dynamics are consistent across both realisations. Initially, the flow begins to run up the barrier, and eventually, it reaches a pseudo-steady-state condition. The diagonal shock wave across the slit is also correctly resolved, hitting the side wall at the correct location. This close match between the numerical and experimental results suggests that the multiscale framework is capable of accurately simulating complex impact, such as that involving a slit/filter barrier.

Figure 8 shows a visualisation of the internal velocity field obtained with the multiscale approach. It demonstrates the effectiveness of the framework, which enables a precise and rich visualisation of the impact. The shape of the free surface is particularly important in the study of impact, because it influences the forces acting on the barrier. The multiscale framework also allows the observation of realistic interactions, including the initial run-up phase, the deflection of streamlines towards the slit aperture, and the formation of a no-flow area at the base of the barrier. It also shows realistic run-up dynamics, with streamlines bending around the impact surface. Notably, this primary information would be lost in the depth-averaging process.

In the flume experiments, the barrier is intentionally designed to be high enough to prevent overflow, allowing for a clear measurement of the run-up height from the side perspex. A comparison between this value and its analogous one

Table 2. Literature review of values used in the μ(I) rheology to describe glass beads, rounded to three decimal places.

Author	μ_s [−]	μ_d [−]	d [mm]	I_0 [−]
Barker and Gray (2017)	0.342	0.554	0.100	0.048
Barker et al. (2015)	0.383	0.643	0.530	0.279
Barker and Gray (2017)	0.342	0.557	0.143	0.069
Barker et al. (2017)	0.532	0.727	0.30	0.517
Barker et al. (2021)	0.367	0.718	2.00	0.517
Chauchat and Médale (2014)	0.383	0.643	0.530	0.279
Fei et al. (2020)	0.278	0.680	0.350	–
Franci and Cremonesi (2019)	0.382	0.644	2.000	0.279
Goddard and Lee (2017)	0.383	0.643	2.000	0.279
Heyman et al. (2017)	0.380	0.644	0.053	0.300
Jianbo et al. (2020)	0.380	0.650	0.250	0.300
Jianbo et al. (2020)	0.380	0.650	0.250	0.300
Jianbo et al. (2020)	0.380	0.650	0.250	0.300
Jop et al. (2005)	0.382	0.644	0.053	0.300
Jop et al. (2006)	0.382	0.644	0.053	0.300
Lacaze and Kerswell (2009)	0.400	0.700	1.000	0.400
Lagrée et al. (2011)	0.380	0.640	1.000	0.400
Mangeney et al. (2010)	0.384	0.645	0.700	0.279
Martin et al. (2017)	0.480	0.760	0.700	0.279
Midi (2004)	0.382	–	0.800	8.480
Midi (2004)	0.382	–	0.800	4.500
Pouliquen and Forterre (2002)	0.384	0.594	0.400	0.279
Tankeo et al. (2013)	0.382	0.644	0.530	0.279
Valette et al. (2019)	0.420	0.600	0.400	0.300
Valette et al. (2019)	0.520	0.700	0.500	0.300
Valette et al. (2019)	0.620	0.800	0.800	0.300
Yang et al. (2023)	0.383	0.640	1.000	0.279

Table 3. Calibrated parameters for the μ(I) rheology, used for back-analysing the laboratory flow.

μ_s	–	0.342
μ_d	–	0.669
I_0	–	0.103
d	mm	0.53
ρ_p	kg/m^3	2470

from the simulations allows evaluating the influence of the subdomain configurations, particularly the location of the interface section. As the barrier blocks 50% of the flume width, the initial shock develops into a granular tidal bore that slowly propagates upstream. Although no established framework is able to precisely predicts its speed, we observed that for $t/t^* < 3$, the bore remains less than 0.05 m upstream from the barrier. This is within the area recorded by the camera. Thus, we test configurations where the interface section is located outside this region: $x_i = 0.10$, 0.20, and 0.30 m upstream of the barrier, respectively. Since these sections are not reached by the tidal bore and the flow remains in supercritical conditions for the entire duration, they should all yield equivalent results.

Figure 9 supports this hypothesis by presenting the combined model results alongside the laboratory data. The numerical results agree with the experimental observations. However, the run-up in the simulations tends to be slightly lower than in the experiments. This discrepancy is likely due to the difficulty in accurately capturing the dynamics of the uppermost, most dispersed section of the run-up, where the mass exhibits a collisional state that LBM, as a constant-density continuum, struggles to reproduce with high fidelity. The comparison also confirms that, within the studied range, the influence of the interface section is indeed negligible.

Figure 9 also presents the impact forces as computed using the multiscale framework. It is important to note that no load cells were installed on the barrier in the laboratory experimental setup; therefore, direct measurements of the impact forces were not recorded. However, the accuracy of LBM in predicting impact forces has been rigorously validated in previous studies. In particular, Ng et al. (2023) performed an independent validation of the same LBM implementation against experimental measurements, demonstrating satisfactory agreement in force predictions.

As in Leonardi et al. (2019), we employ an analytical approach to verify that the method provides realistic estimations and to compare results using different domain decom-

Fig. 6. Numerical results of flow velocity and flow depth: (*a*) 3D framework at 28°, (*b*) DA framework at 28°, (*c*) 3D framework at 30°, (*d*) DA framework at 30°. All results are scaled by the reference velocity $\bar{u}^*$ and flow depth h^* for both 28° and 30° scenarios.

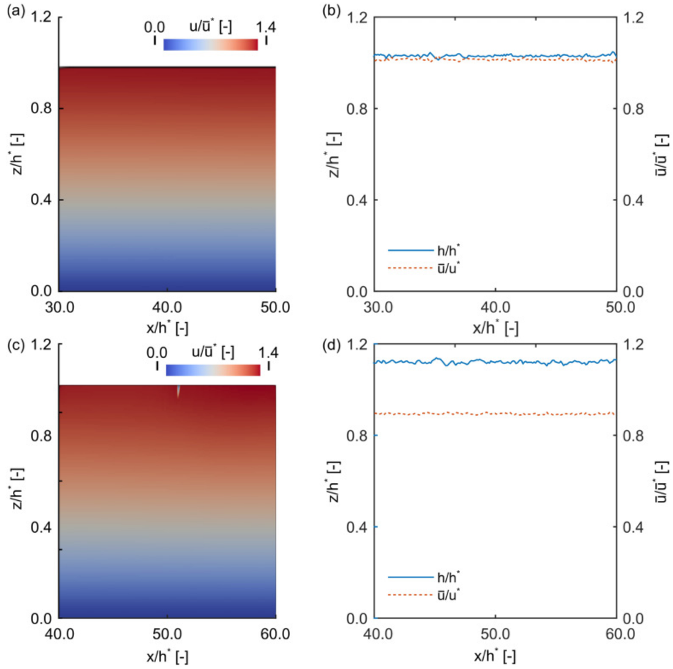

position. Just before impact, a Froude number $\mathrm{Fr} = \bar{u}^*/\sqrt{gh^*}$ of 1.4 and 2.1, for 28° and 30° simulations, respectively, is recorded. This suggests that a hydrodynamic approach is suitable, and consequently impact forces are scaled using the stagnation pressure:

$$k = \frac{F}{\rho \bar{u}^{*2} W_\mathrm{w} h^*} \qquad (21)$$

where W_w is the width of the barrier and F is the resultant force acting on the barrier. The reference flow depth of undisturbed flow h^* and the corresponding depth-averaged velocity $\bar{u}^*$ are presented in Table 1. The results, shown in Fig. 9, indicate that the framework predicts impact coefficients k close to unity, as expected.

The numerical framework results, across different subdomain configurations, once again show good agreement. Regardless of the interface section location, the forces generally follow the same time history for a given slope angle. This underscores a key advantage of the multiscale approach, enabling accurate force computation without needing to model the entire domain in 3D, or to simplify the boundary conditions.

Considerations on the computational efficiency analyses

The computational efficiency of the combined model is compared to that of the DA model. Table 4 reports the computational time required for each analysis. The feasibility of a full 3D LBM analysis primarily depends on the number of lattice points to be solved, particularly along the flow height. Based on the authors' experience, a resolution of 15 to 20 points is necessary to accurately resolve the fluid along the flow height. For the studied problem, this condition requires a lattice discretisation of approximately 0.8 mm. Solving the entire domain with a full 3D LBM model would involve approximately $30 \cdot 10^6$ computational points. For a typical CPU computer, it is computationally prohibitive. The 3D model can be optimised but the computational cost might be prohibitive anyway. Hence, in this work the combined model is proposed as an alternative to a brute force 3D solver. In this way, the computational resources required are reduced. Table 4 reports results from the DA and combined models. The data highlights that computational time increases with the number of nodes to be solved by the 3D subdomain. The 3D-DA method offers a practical balance between the capability of the DA model capability for flow propagation and the detailed study of the 3D model of the impact analysis. Ultimately, the 3D subdomain represents the real computational bottleneck, significantly slowing down the overall analysis.

Site scale

The multiscale framework, validated in the previous chapter, is applied at the site scale to study the 9 June 2016 event in Saint-Vincent (Leonardi et al. 2021). This poses significant challenges to modelling: in this case, a standalone 3D approach would have been possible only at the expense of accuracy. On the other hand, one could use a DA model to solve the whole problem, including the impact. DA models have been proven to be efficient to solve large basin areas (Mangeney-Castelnau 2003; Pirulli and Sorbino 2008; Pastor et al. 2015), thanks to hypotheses that simplify the governing equations without giving up efficiency for studying debris flows and avalanches. The primary assumption is the shallow-flow hypothesis, which considers the flow depth to be much smaller than the characteristic horizontal length scale. This leads to the depth-averaging of the governing equations, effectively removing vertical velocity variations (Gray et al. 1999). Another hypothesis is that the flow behaves as a continuum, in this work it is modelled as a single-phase material with an effective rheology. Finally, DA models assume that the resistance to flow is located solely at the interface between the topography surface and the flow. While these assumptions enable the efficient modelling of large-scale flows, they introduce significant limitations. The omission of vertical velocity components prevents DA models from capturing the internal shear stress distribution and momentum transfer in the vertical direction, which are crucial in understanding impacts with structures. The DA model employed, despite the mentioned limitations, remains consistent with the underlying assumptions of depth-averaged approaches and is a suitable candidate for investigating the propagation phase of the studied event.

Model setup

Figures 3c and 3d highlight the different meshes used in the two subdomains. The DA subdomain is discretised using an unstructured mesh with 5.0 m spacing, balancing accu-

Fig. 7. Free surface shape: Experimental results at 28° (*a*–*d*) and 30° (*i*–*l*), with corresponding views from the simulation data (*e*–*h*, *m*–*p*). The black dashed line represents the shape of the free surface near the flume sidewall, intended for comparison with the numerical results. Distances on the x and y axes are scaled by the reference flow depth h^*. All results correspond to the case where the interface section is located $0.30\,\mathrm{m}/h^*$ upstream from the barrier. The time is scaled using the time of first impact t_0 and the reference timescale t^*. The dashed line represents the free surface at the closest sidewall to the camera.

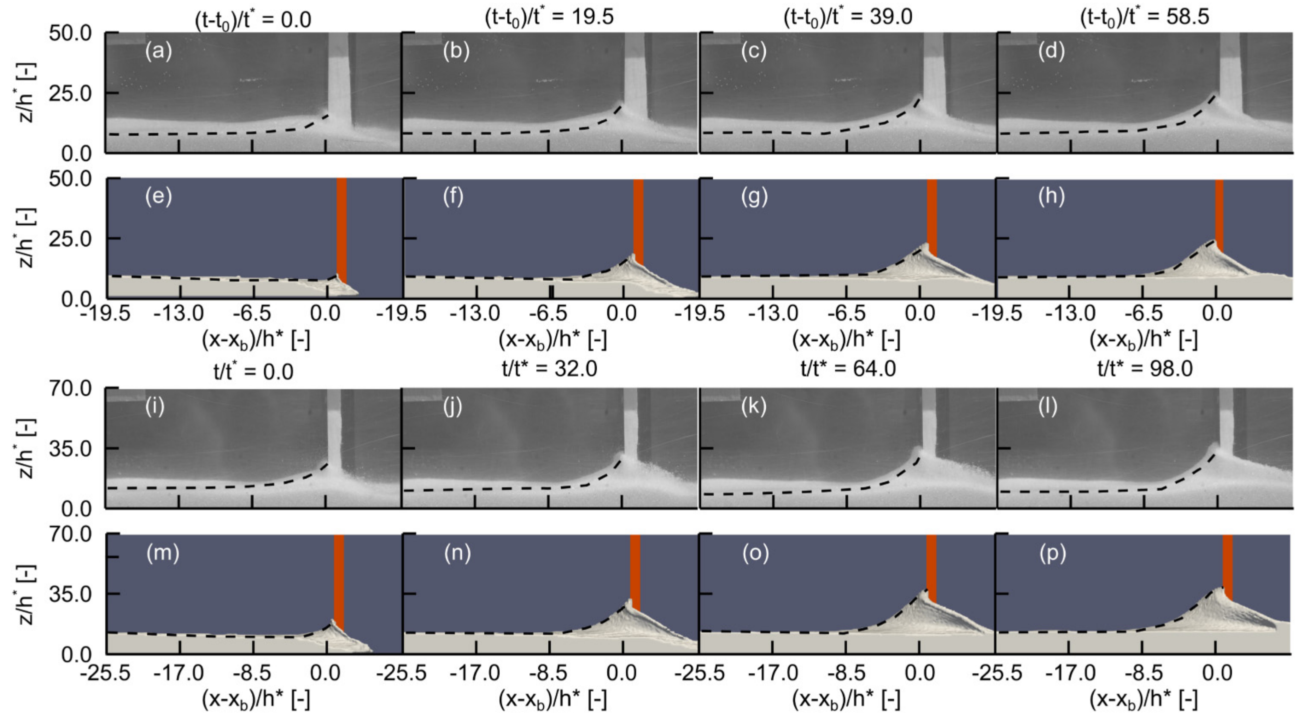

racy with computational efficiency. The calibration was performed through a back analysis of the 9 June 2016 event, where the friction coefficient μ and turbulence coefficient ξ were calibrated within ranges of 0.1–0.2 and 100–$100\,\mathrm{m/s^2}$, respectively. The best-fit parameters ($\mu = 0.2$, $\xi = 500\,\mathrm{m/s^2}$) were determined by comparing numerical results with observed data, including flow velocity from video analysis and deposit dimensions. The complete procedure of the calibration is discussed in Leonardi et al. (2021). In contrast, the 3D model uses a finer mesh of 0.05 m lattice spacing and a time step of $1 \cdot 10^{-5}$ s. Figure 10*a* presents a detailed satellite image of the channel close to the barrier, with the 3D subdomain highlighted in orange. This subdomain covers approximately $220\,\mathrm{m}^2$. Within this area, the channel is maintained by the local authority, and has a roughly constant slope fixed at 13°. Therefore, the 3D geometry can be simplified as a simple orthogonal channel with constant slope. Figures 10*b* and 10*c* depict the numerical resolution of the channel, including the boundary conditions for the 3D subdomain and the position of the barrier.

In this study, the multiscale framework is applied to analyse the interaction between debris flows and the monitored filter barrier, with particular emphasis on the 3D subdomain. Details of the calibration process for the DA model are provided in the back-analysis performed by Leonardi et al. (2021). They found that a model based on a Voellmy rheology with parameters $\mu = 0.2$ and $\xi = 500\,\mathrm{m/s^2}$ yielded an excellent back-analysis. These values are also consistent with the literature (Meyrat et al. 2023; Mitchell et al. 2022).

To ensure consistency between the models, this study employs the unified description of the Voellmy rheology. The DA rheological parameters from Leonardi et al. (2021) are used as a base to compute equivalent 3D parameters, following the approach previously outlined: μ remains unchanged, while l^* is computed using eq. 16. The resulting rheological parameters for the 3D subdomain are $\mu = 0.2$ and $l^* = 0.0672\,\mathrm{m}$. Equation 16 requires the definition of a characteristic length scale for the flow. Here, the average flow height at the location of the interface section is chosen, which corresponds to $h^* = 1.20\,\mathrm{m}$. This characteristic flow height is also chosen to scale the results, together with the time at first impact t_0.

Figure 11 displays four frames from the simulation of a debris flow impacting the filter barrier. These frames illustrate the sequential stages of the flow as it enters the 3D subdomain, impacts the barrier, and then seeps through the steel beams. This is the mechanism prescribed in the design and observed on site (Leonardi et al. 2021). Panel (a) shows the initial entry of the debris flow into the 3D subdomain, with the flow approaching the barrier at $t = -1.0\,\mathrm{s}$. Panel (b) depicts the first instant of impact at $t = t_0 = 0.0\,\mathrm{s}$, where the flow begins to interact with the barrier and run-up initiates. Note that the concrete base of the dam is impervious to the flow. Panel (c) captures the flow at $t = 1.0\,\mathrm{s}$, showing the material starting to cross the filter. Finally, panel (d), at $t = 2.0\,\mathrm{s}$, shows the continued passage of material through the bar-

Fig. 8. Visualisation of the free surface of the flow (shaded grey area) and the velocity streamlines for the $\theta = 28^\circ$ (*a*–*f*) and $\theta = 30^\circ$ (*g*–*l*) flows. All results refer to the case where the interface section is located 0.30 m/h^* upstream from the barrier. The time is scaled using the time of first impact t_0 and the reference timescale t^*.

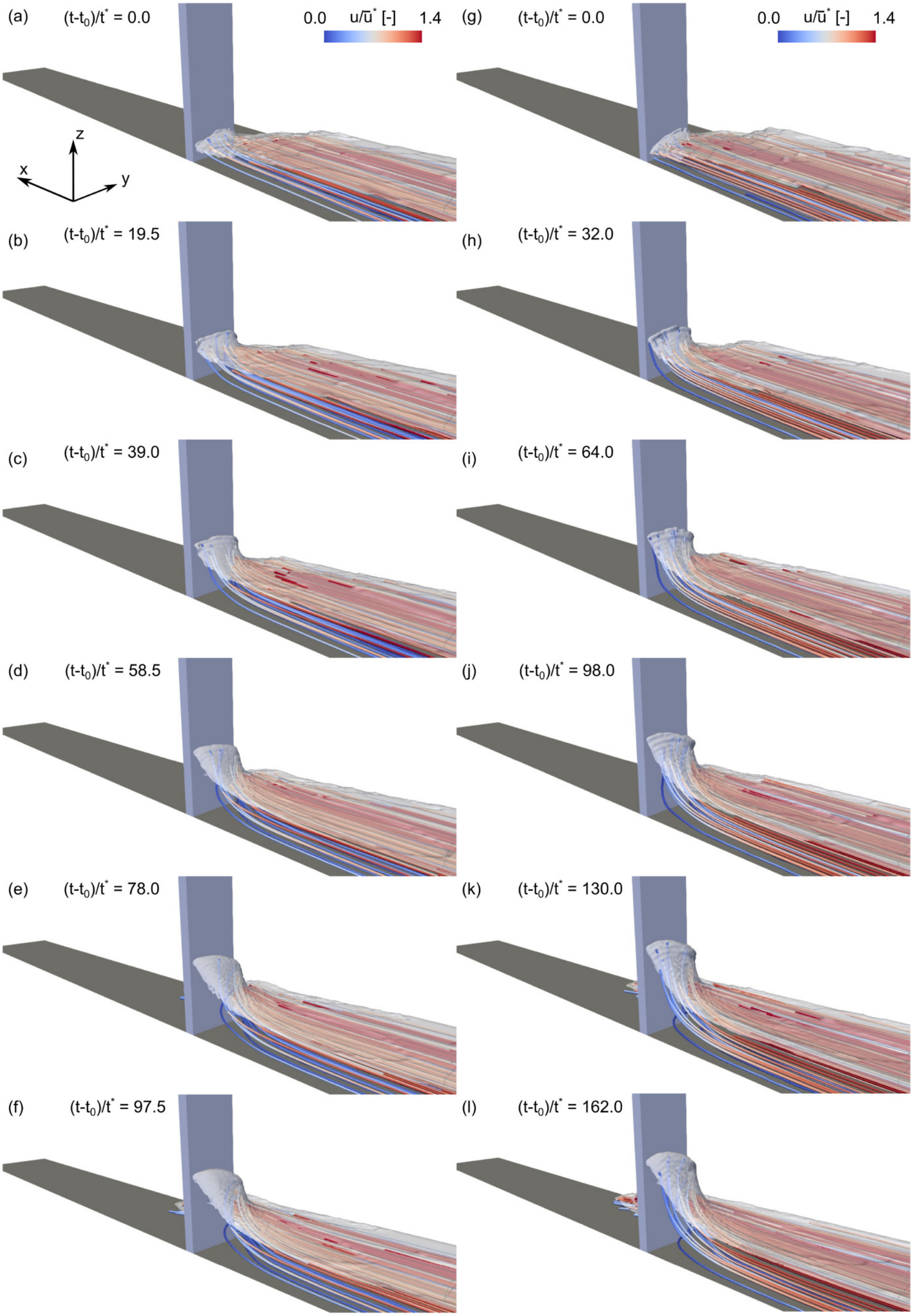

Fig. 9. Comparison of experimental and numerical results for run-up height h_r. The experimental data for run-up at $\theta = 28°$ (diamonds) and $\theta = 30°$ (circles) are displayed alongside the numerical results for both slope angles. Additionally, the dimensionless force coefficient k is included for both slope angles. The time is scaled using the time of first impact t_0 and the reference timescale t^*.

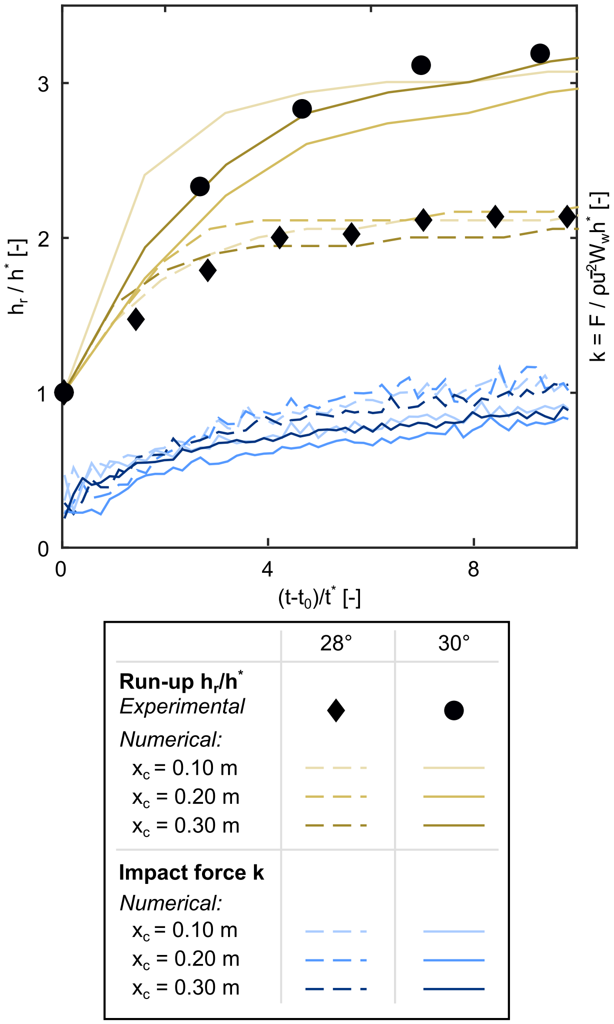

Table 4. Computational time for DA and combined model.

Model	Nodes 3D	Time (h) 28°	Time (h) 30°
DA	N/A	0.04	0.05
DA-3D (0.10 m)	$5.9 \cdot 10^6$	71.03	49.30
DA-3D (0.20 m)	$6.8 \cdot 10^6$	86.12	67.73
DA-3D (0.30 m)	$7.8 \cdot 10^6$	112.68	106.68

rier, with a portion of the debris flow filtering through the beams. The results are promising: the sequence shows a natural progression from impact to filtering, with the material passing through the barrier as expected. This validates the ability of the framework to accurately simulate the interaction between the debris flow and the filter barrier, with the impact followed by appropriate material behaviour as per the design specifications.

Fig. 10. St. Vincent case study: (*a*) channel where the debris flow occurred, featuring the visible barrier and the area studied by the 3D model highlighted in orange. (*b*) Planar view of the numerical model, illustrating the numerical scheme along with the boundary conditions. (*c*) 3D numerical sketch indicating the relevant distances.

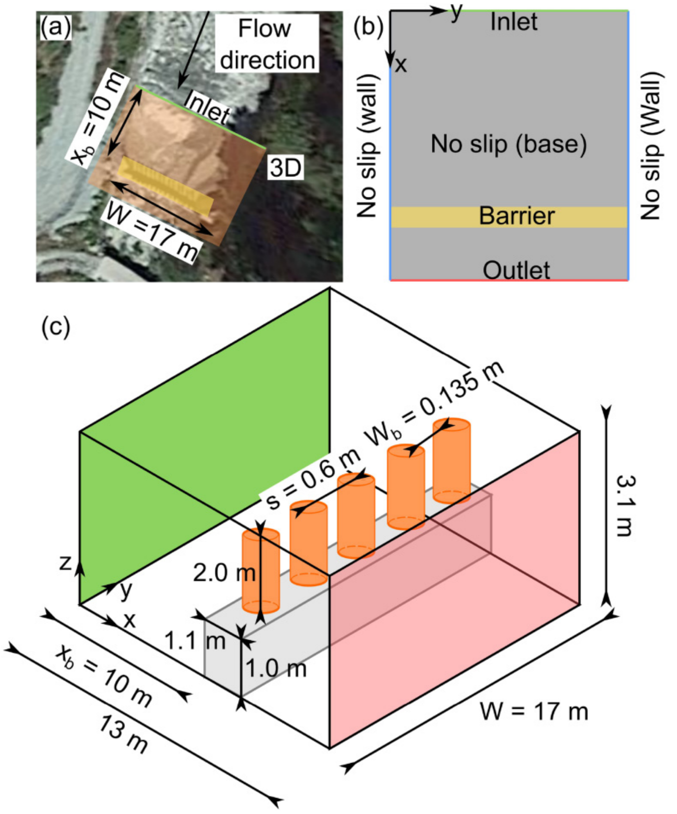

Figures 12*a*–12*d* show the flow structure at a central section of the channel. These frames confirm the mechanisms discussed in the previous section, namely the processes of impact, run-up, and lamination of the flow. The velocities obtained from the 3D component of the model are consistent with the observations reported by Leonardi et al. (2021), where the authors documented velocities ranging between 2.0 and 2.6 m/s. Additionally, the impact depicted in the figure allows for the observation of momentum transfer in the vertical direction, as evidenced by the vertical component of the velocity vectors. Notably, this aspect could not be observed in the study by Leonardi et al. (2021), as they employed a standalone DA model.

Figures 12*e*–12*h* present a planar view of the channel, focusing on the central area near the filter. The vectors represent the velocity at the free surface. It is noteworthy to observe the interaction between the flow and the beams. After the first two frames, where the initial impact and run-up occur, the material begins to flow through the filter barrier. This behaviour aligns with the intended design of the barrier, which is meant to dissipate the flow energy without completely inducing stoppage. The impact in this case captures more details than those reported by Leonardi et al. (2021), particularly because the interaction between the flow and the beams is

Fig. 11. Rendering of simulation of the St. Vincent case study, with focus on the 3D subdomain. The panels illustrate the flow transitioning through the interface section and into the 3D subdomain, and its behaviour following impact with the barrier.

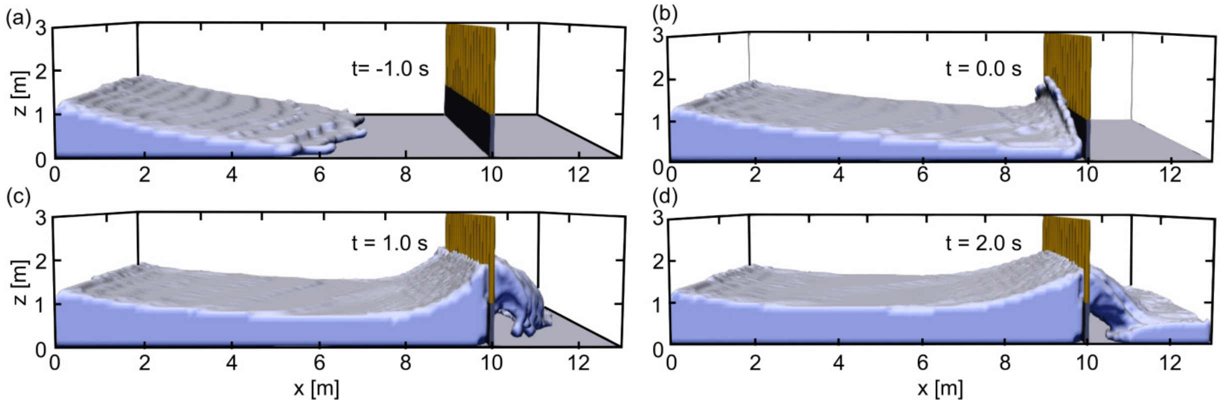

influenced by the vertical momentum transfer observed in panel (f), which is neglected in the standalone DA model.

The figure also highlights how the multiscale framework makes an optimised use of computational resources. Capturing impact with this level of resolution with a standalone 3D model would be prohibitively challenging, either due to the computational cost or due to an oversimplification of boundary conditions. Furthermore, the impact is in this case consistent with the flow structure obtained from runout analysis in the DA subdomain.

Figure 13 presents the forces acting on the beams of the studied filter barrier (refer to Fig. 10). Some of the forces appear negative because they are back-calculated from strain measurements on the beams, which sometimes show tension instead of the expected compression. This happens due to uneven and localised impacts from large debris particles, which can clog the barrier openings and push against the beams from the side, causing them to bend in multiple directions (Leonardi and Pirulli 2020). These side-on, or lateral, loads introduce bi-axial bending and lead to tensile strains at certain sensor locations, especially when boulders get lodged between beams. However, the strains from lateral loads are generally small compared to those from the main flow direction, and when data from all beams are considered together, the overall pattern remains clear—so these effects are treated as background noise rather than dominant behaviour (Leonardi et al. 2021). The monitoring system collected beam deformations at a frequency of 1 Hz. Although this frequency is not highly detailed, it provides sufficient information to reconstruct the deformation history of the beams. Leonardi et al. (2021) used the deformation data to estimate the forces acting on the beams, employing elastic theory and assuming a uniform load across the beam surfaces. The solid grey lines with markers represent the forces computed in this way. Some of the field data related to the beams are not reported in the figure due to the presence of boulders that caused an arching effect due to clogging. In such cases, the forces are not solely compressive (positive) but also tensile (negative), as demonstrated by Leonardi and Pirulli (2020). Since the numerical model discussed in this study is based on a continuum framework, it cannot capture the effects due to boulders and arch effect. Hence, field data from beams experiencing the arching effect are not included in the comparison, as they are not directly comparable with the continuum model results. In the same figure, the mean value across all beams is shown as a solid black line, which highlights the overall force trends. The mean numerical value is depicted as an orange solid line. The numerical results are recorded at a significantly higher frequency (200 Hz) to capture the force history more accurately, allowing for the detection of any peaks or plateaus during the simulation. The forces are scaled using hydrodynamic principles. In this context, the reference flow velocity, $\bar{u}^*$, is assumed to be 2.5 m/s, based on the observations reported by Leonardi et al. (2021). The same study identifies the reference flow depth as $h^* = 1.2$ m. This results in a reference time scale of $t^* = 0.48$ s.

Despite some discrepancies between the numerical results and the mean field data, the models appear to capture the overall trend of the forces effectively. Both the average field data and the numerical results exhibit an initial phase where the forces increase slowly, followed by a period of roughly steady growth. This trend can be attributed to the debris flow initially impacting the base of the slit dam, an area where data was not recorded due to the absence of strain gauges. As the volume upstream of the barrier is gradually filled, the debris flow began to exert force against the beams, resulting in a roughly constant increase in force. The general agreement suggests that the numerical model is effectively capturing key dynamics of the debris flow and its interaction with the beams, particularly under the unsteady conditions of the field study.

While the results presented in this work demonstrate the effectiveness of the combined model, several limitations remain that should be addressed in future developments. One key limitation concerns the one-way transfer of information from the DA model to the 3D model. Currently, the framework only allows data to flow in this direction, which restricts its applicability to supercritical flows, where upstream conditions dictate the downstream flow behaviour. In such cases, the placement of the interface section does not impact the results, as the flow perturbations do not propagate upstream. However, the model cannot yet handle subcriti-

Fig. 12. (*a–d*) Flow velocity at the central section of the channel, with insets illustrating the flow impact against the barrier and the corresponding velocities. (*e–h*) Planar view of the central area of the channel, showing velocity vectors at the free surface.

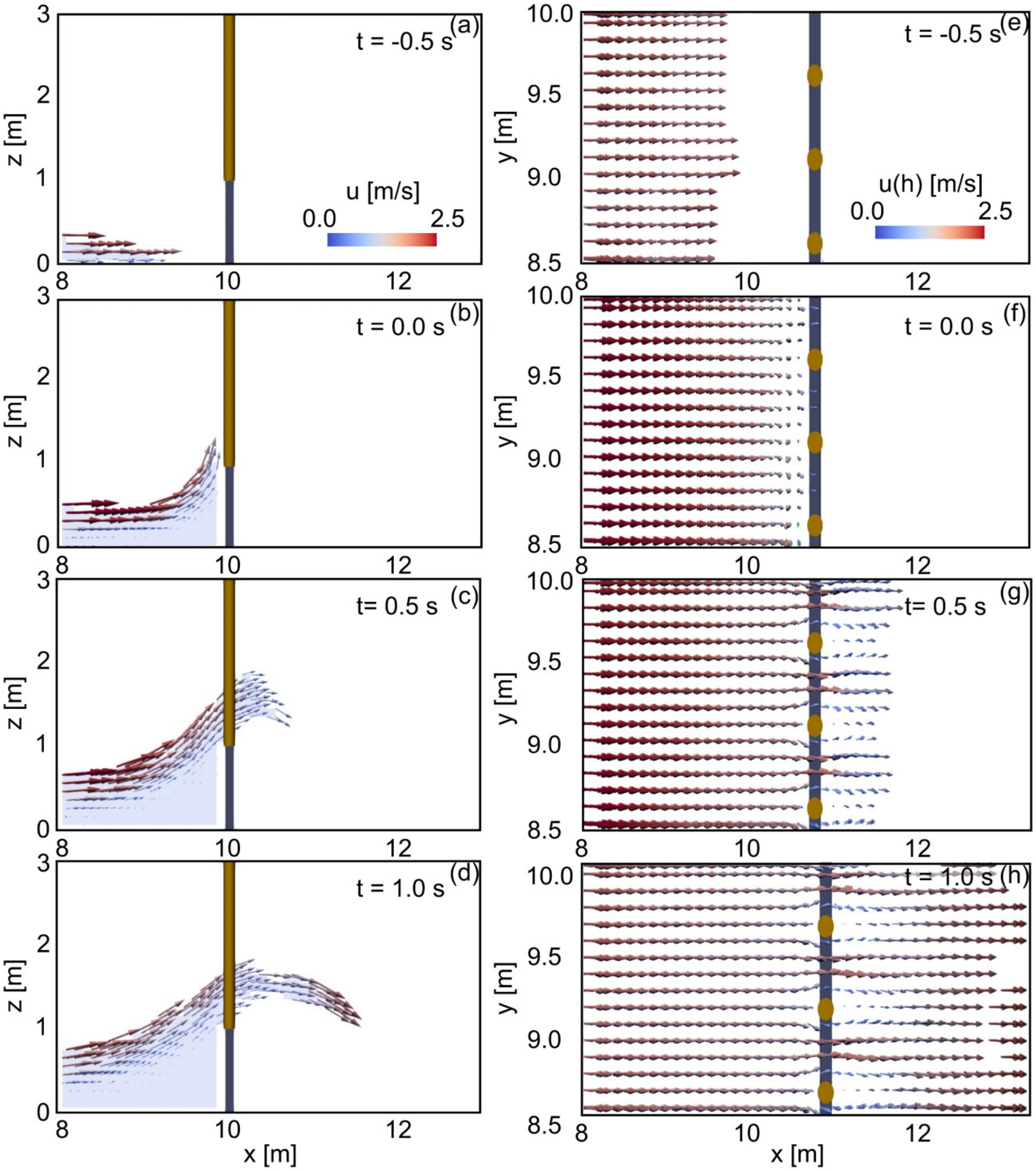

cal flows, where sudden changes in topography may generate reflected waves travelling upstream. If these waves reach the interface section, the current approach fails to account for their influence, as no information is passed from the 3D model back to the DA model. To extend the framework to such scenarios, new boundary conditions must be developed, enabling a truly two-way coupled DA-3D model. Another limitation is the current inability of the model to account for boulder-rich flows. The present approach assumes either a purely fluid-like flow or a scenario where only a limited number of boulders are present. However, in natural debris flows, the presence of boulders can significantly alter flow dynamics, leading to particle segregation and size sorting effects. Addressing this issue would require coupling the 3D LBM model with the Discrete Element Method (DEM), an approach successfully implemented in previous studies (Leonardi et al. 2014) to simulate fluid-solid interactions. Future work should focus on addressing these limitations.

Conclusions

This study introduces a novel multiscale framework for simulating debris flows and their impact on mitigation structures. By combining DA models for flow propagation with a 3D solver for impact. This approach optimises computational resources without sacrificing accuracy. The framework is in principle solver-agnostic, meaning that it is the same principles that can be applied to any 3D model for frictional flows,

Fig. 13. Dimensionless force coefficient k: field data and numerical results. The time is scaled using the time of first impact t_0 and the reference time scale of flow, t^*.

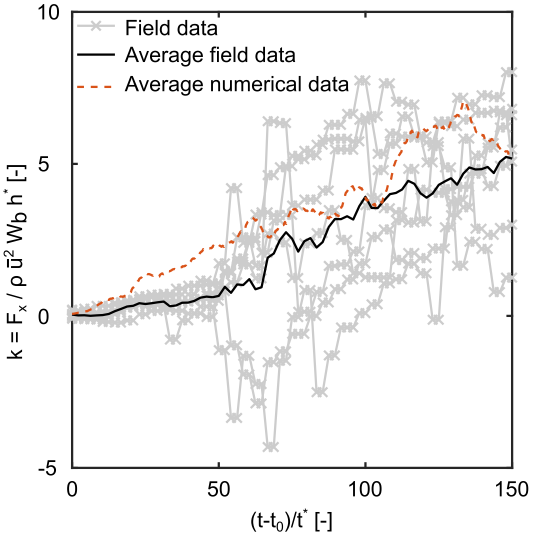

offering broad applicability across the many different tools currently under development.

The proposed multiscale framework is the first of its kind to apply this multiscale approach at the site scale, and it enables researchers and practitioners to simulate full runout and impact sequences in one framework, a capability that had previously remained fragmented or theoretical. It effectively overcomes the limitations of traditional methods, which often rely on simplified release mechanisms like dam-break schemes. These often introduce uncertainties that are difficult to quantify. By employing a DA model for the upstream flow and transitioning to 3D models only in regions of interest, such as the near-field of mitigation structures, this framework avoids these uncertainties and provides more reliable results. This includes an estimation of the forces acting on structures and the detailed shape of the flow structure.

Validation of the framework has been first conducted at the laboratory scale. It shows that with the current combining algorithm for supercritical flows, the position of the interface section has no significant influence on results. The experiments highlight the ability of the framework to simulate key features such as run-up, flow structure, and impact forces with accuracy. The application of the multiscale framework to a real-world debris flow event in the Italian Alps further demonstrated its potential. Although site-scale quantitative validation was limited to force measurements on a filter barrier, the results were qualitatively promising, aligning well with field observations and reinforcing the framework's capability to handle complex, natural environments.

A key innovation of this study is a unified implementation of the Voellmy rheology within a DA-3D framework. This widely accepted model, typically used in DA simulations, has been adapted for 3D use, simplifying the calibration process by requiring only two parameters. This is a significant improvement over models like the μ(I) rheology, which requires more complex calibration and is limited to dry granular flows—conditions rarely met at the site scale. The successful application of Voellmy rheology within the multiscale framework opens the door for future research and practical applications in geotechnical and hazard mitigation contexts, supporting improved design of protective infrastructure, enabling more robust back-analysis of past events, and offering a pathway toward operational simulation tools for early warning and hazard planning.

Looking ahead, this framework holds strong potential for future enhancements, particularly through the inclusion of discrete particles immersed in the 3D continuum. A hybrid continuum-discrete approach could enable the simulation of blockage and clogging phenomena, which are currently difficult to capture using pure-continuum models. Further validation under a wider range of conditions, including different material compositions and larger-scale events.

List of symbols

c_s	lattice sound velocity
c_i	discretised velocities
d	numerical particle diameter
d_p	particle diameter
Fr	Froude number
f_i	probability function
f_i^{eq}	equilibrium probability function
$\mathbf{g}$	gravity acceleration
h	flow depth
h_r	run-up height
h^*	reference flow depth
I	inertial number
I_0	material constant
I_θ	inertial number slope-specific
L^*	characteristic dimensionless thickness
k	dynamic empirical force parameter
p	pressure
Q	discharge
s	beams spacing
t	time
t_0	first time impact
t_r	relaxation time
t^*	reference time scale of flow
$\bar{u}_i$	depth-averaged velocity in the i-component
$\bar{u}^*$	reference flow velocity
$\boldsymbol{u}_i$	flow velocity in the i-component
W	width of the studied problem
W_b	width of the beam
W_w	width of the barrier in the flume
$\mathbf{x}$	space vector (x, y, and z components)
x_b	inlet-barrier distance
x_i	position of the interface section
β	material constant
$\dot{\gamma}$	shear rate
Δt	time step
Δx	lattice spacing
θ	slope inclination
μ	frictional coefficient
μ_d	dynamic frictional coefficient
μ_s	static frictional coefficient

ν	kinematic viscosity
ξ	velocity-dependant dissipation
ρ	flow density
ρ_p	particle density
τ_b	basal shear resistance
Ω_i	collision operator

Acknowledgements

A part of this study was carried out within the RETURN Extended Partnership and received funding from the European Union Next-GenerationEU (National Recovery and Resilience Plan—NRRP, Mission 4 Component 2, Investment 1.3—D.D. 1243 2/8/2022, PE0000005)—SPOKE VS 2.

Article information

History dates

Received: 13 January 2025
Accepted: 30 May 2025
Version of record online: 29 July 2025

Copyright

Data availability

Data generated or analyzed during this study are available from Aosta Valley Region. Data are, however, available from the authors upon reasonable request and with permission of Aosta Valley Region.

Author information

Author ORCIDs

A. Pasqua https://orcid.org/0000-0002-6089-4857

Author contributions

Conceptualization: AP
Funding acquisition: MP
Methodology: AL
Supervision: AL, MP
Validation: AP, MP
Writing – original draft: AP
Writing – review & editing: AL, MP

Competing interests

The authors declare there are no competing interests.

References

Ashwood, W., and Hungr, O. 2016. Estimating total resisting force in flexible barrier impacted by a granular avalanche using physical and numerical modeling. Canadian Geotechnical Journal, **53**(10): 1700–1717. doi:10.1139/cgj-2015-0481.

Bagnold, R.A. 1954. Experiments on a gravity-free dispersion of large solid spheres in a Newtonian fluid under shear. Proceeding of the Royal Society of London Series A. Mathematical or Physical Science, **225**(1160): 49–63. doi:10.1098/rspa.1954.0186.

Barker, T., and Gray, J.M. 2017. Partial regularisation of the incompressible μ(I)-rheology for granular flow. Journal of Fluid Mechanics, **828**: 5–32. doi:10.1017/jfm.2017.428.

Barker, T., Schaeffer, D.G., Bohorquez, P., and Gray, J.M. 2015. Well-posed and ill-posed behaviour of the μ-rheology for granular flow. Journal of Fluid Mechanics, **779**: 794–818. doi:10.1017/jfm.2015.412.

Barker, T., Schaeffer, D.G., Shearer, M., and Gray, J.M. 2017. Well-posed continuum equations for granular flow with compressibility and (I)-rheology. Proceeding of the Royal Society A. Mathematical or Physical Engineering Science, **473**(2201). doi:10.1098/rspa.2016.0846.

Barker, T., Rauter, M., Maguire, E.S., Johnson, C.G., and Gray, J.M. 2021. Coupling rheology and segregation in granular flows. Journal of Fluid Mechanics, **909**. doi:10.1017/jfm.2020.973.

Bhatnagar, P.L., Gross, E.P., and Krook, M. 1954. A model for collision processes in gases. I. Small amplitude processes in charged and neutral one-component systems. Physical Review, **94**(3): 511–525. doi:10.1103/PhysRev.94.511.

Chauchat, J., and Médale, M. 2014. A three-dimensional numerical model for dense granular flows based on the μ(I) rheology. Journal of Computer Physics, **256**: 696–712. doi:10.1016/j.jcp.2013.09.004.

Chen, H.X., Li, J., Feng, S.J., Gao, H.Y., and Zhang, D.M. 2019. Simulation of interactions between debris flow and check dams on three-dimensional terrain. Engineering Geology, **251**(January): 48–62. doi:10.1016/j.enggeo.2019.02.001.

Cuomo, S., Di Perna, A., and Martinelli, M. 2021. Material point method (MPM) hydro-mechanical modelling of flows impacting rigid walls. Canadian Geotechnical Journal, **58**(11): 1730–1743. doi:10.1139/cgj-2020-0344.

D'Aosta, R.A.V. 2019. Cartography data: CTRR.

Domnik, B., Pudasaini, S.P., Katzenbach, R., and Miller, S.A. 2013. Coupling of full two-dimensional and depth-averaged models for granular flows. Journal of Non-Newtonian Fluid Mechanics, **201**: 56–68. doi:10.1016/j.jnnfm.2013.07.005.

Faug, T. 2015. Depth-averaged analytic solutions for free-surface granular flows impacting rigid walls down inclines. Physical Review E – Statistical Nonlinear, Soft Matter Physics, **92**(6): 1–14. doi:10.1103/PhysRevE.92.062310.

Fei, J., Jie, Y., Zhao, D., and Zhang, B. 2020. Simulation of natural shallow avalanches with the μ(I) rheology. Bulletin of Engineering Geology and the Environment, **79**(8): 4123–4134. doi:10.1007/s10064-020-01821-y.

Forterre, Y., and Pouliquen, O. 2002. Stability analysis of rapid granular chute flows: formation of longitudinal vortices. Journal of Fluid Mechanics, **467**: 361–387. doi:10.1017/S0022112002001581.

Franci, A., and Cremonesi, M. 2019. 3D regularized μ(I)-rheology for granular flows simulation. Journal of Computer Physics, **378**: 257–277. doi:10.1016/j.jcp.2018.11.011.

Furuichi, M., and Nishiura, D. 2017. Iterative load-balancing method with multigrid level relaxation for particle simulation with short-range interactions. Computer Physics Communications, **219**: 135–148. doi:10.1016/j.cpc.2017.05.015.

García-Delgado, H., Machuca, S., and Medina, E. 2019. Dynamic and geomorphic characterizations of the Mocoa debris flow (March 31, 2017, Putumayo Department, southern Colombia). Landslides, **16**(3): 597–609. doi:10.1007/s10346-018-01121-3.

Goddard, J.D., and Lee, J. 2017. On the stability of the μ(I) rheology for granular flow. Journal of Fluid Mechanics, **833**: 302–331. doi:10.1017/jfm.2017.651.

Gray, J.M., and Edwards, A.N. 2014. A depth-averaged μ(I)-rheology for shallow granular free-surface flows. Journal of Fluid Mechanics, **755**(4): 503–534. doi:10.1017/jfm.2014.450.

Gray, J.M., Wieland, M., and Hutter, K. 1999. Gravity-driven free surface flow of granular avalanches over complex basal topography. Proceeding of the Royal Society A. Mathematical or Physical Engineering Science, **455**(1985): 1841–1874. doi:10.1098/rspa.1999.0383.

Habich, J., Feichtinger, C., Köstler, H., Hager, G., and Wellein, G. 2013. Performance engineering for the lattice Boltzmann method on GPGPUs: Architectural requirements and performance results. Computers & Fluids, **80**(1): 276–282. doi:10.1016/j.compfluid.2012.02.013.

Heyman, J., Delannay, R., Tabuteau, H., and Valance, A. 2017. Compressibility regularizes the μ(I)-rheology for dense granular flows. Journal of Fluid Mechanics, **830**: 553–568. doi:10.1017/jfm.2017.612.

Hübl, J., Nagl, G., Suda, J., and Rudolf-Miklau, F. 2017. Standardized stress model for design of torrential barriers under impact by debris flow (according to Austrian standard regulation 24801). International Journal Erosion Control Engineering, **10**(1): 47–55. doi:10.13101/ijece.10.47.

Iverson, R.M. 1997. The physics of debris flows. Review Geophysics, **35**(3): 245–296. doi:10.1029/97RG00426;.

Iverson, R.M. 2015. Scaling and design of landslide and debris-flow experiments. Geomorphology, **244**: 9–20. doi:10.1016/j.geomorph.2015.02.033.

Iverson, R.M., Logan, M., Lahusen, R.G., and Berti, M. 2010. The perfect debris flow? Aggregated results from 28 large-scale experiments. Journal of Geophysical Research-Earth Surface, **115**(F3): 1–29. doi:10.1029/2009JF001514.

Jianbo, F., Yuxin, J., Xiaohui, S., and Xi, C. 2020. Experimental investigation on granular flow past baffle piles and numerical simulation using a μ(I)-rheology-based approach. Powder Technology, **359**: 36–46. doi:10.1016/j.powtec.2019.09.069.

Jop, P., Forterre, Y., and Pouliquen, O. 2005. Crucial role of sidewalls in granular surface flows: consequences for the rheology. Journal of Fluid Mechanics, **541**(i): 167–192. doi:10.1017/S0022112005005987.

Jop, P., Forterre, Y., and Pouliquen, O. 2006. A constitutive law for dense granular flows. Nature, **441**(7094): 727–730. doi:10.1038/nature04801.

Körner, C., Pohl, T., Rüde, U., Thürey, N., and Zeiser, T. 2006. Parallel lattice Boltzmann methods for CFD applications. Lectures Notes Computer Science Engineering, **51**: 440–466. doi:10.1007/3-540-31619-1_13.

Kumar, V., Gupta, V., Jamir, I., and Chattoraj, S.L. 2019. Evaluation of potential landslide damming: case study of Urni landslide, Kinnaur, Satluj valley, India. Geoscience Frontiers, **10**(2): 753–767. doi:10.1016/j.gsf.2018.05.004.

Lacaze, L., and Kerswell, R.R. 2009. Axisymmetric granular collapse: a transient 3D flow test of viscoplasticity. Physical Review Letters, **102**(10): 3–6. doi:10.1103/PhysRevLett.102.108305.

Lagrée, P.Y., Staron, L., and Popinet, S. 2011. The granular column collapse as a continuum: validity of a two-dimensional Navier-Stokes model with a μ(I)-rheology. Journal of Fluid Mechanics, **686**: 378–408. doi:10.1017/jfm.2011.335.

Larsen, M., Wieczorek, G., Eaton, L., and Torres-Sierra, H. 2001. Natural hazards on alluvial fans: the debris flow and flash flood disaster of December 1999, Vargas State, Venezuela the Debris Flow and Flash Flood Disaster of December 1999, Vargas State, Venezuela. Proceedings: Sixth Caribbean Islands Water Resource Congress, **00965**(December 1999): 1–7.

Leonardi, A., and Pirulli, M. 2020. Analysis of the load exerted by debris flows on filter barriers: comparison between numerical results and field measurements. Computers and Geotechnics **118**(October 2019): 103311. doi:10.1016/j.compgeo.2019.103311.

Leonardi, A., Wittel, F.K., Mendoza, M., and Herrmann, H.J. 2014. Coupled DEM-LBM method for the free-surface simulation of heterogeneous suspensions. Computational Particle Mechanics, **1**(1): 3–13. doi:10.1007/s40571-014-0001-z.

Leonardi, A., Wittel, F.K., Mendoza, M., Vetter, R., and Herrmann, H.J. 2016. Particle-fluid-structure interaction for debris flow impact on flexible barriers. Computer Civil and Infrastructure Engineering, **31**(5): 323–333. doi:10.1111/mice.12165.

Leonardi, A., Goodwin, G.R., and Pirulli, M. 2019. The force exerted by granular flows on slit dams. Acta Geotechnica, **14**(6): 1949–1963. doi:10.1007/s11440-019-00842-6.

Leonardi, A., et al. 2021. Impact of debris flows on filter barriers: analysis based on site monitoring data. Environmental & Engineering Geoscience, **27**(2): 195–212. doi:10.2113/EEG-D-20-00013.

Llano-Serna, M.A., Farias, M.M., and Pedroso, D.M. 2016. An assessment of the material point method for modelling large scale run-out processes in landslides. Landslides, **13**(5): 1057–1066. doi:10.1007/s10346-015-0664-4.

Mangeney, A., Roche, O., Hungr, O., Mangold, N., Faccanoni, G., and Lucas, A. 2010. Erosion and mobility in granular collapse over sloping beds. Journal of Geophysical Research-Earth Surface, **115**(3): 1–21. doi:10.1029/2009JF001462.

Mangeney-Castelnau, A. 2003. Numerical modeling of avalanches based on Saint Venant equations using a kinetic scheme. Journal of Geophysical Research, **108**(B11): 1–18. doi:10.1029/2002jb002024.

Marchelli, M., Leonardi, A., Pirulli, M., and Scavia, C. 2020. On the efficiency of slit-check dams in retaining granular flows. Geotechnique, **70**(3): 226–237. doi:10.1680/jgeot.18.P.044.

Martin, N., Ionescu, I.R., Mangeney, A., Bouchut, F., and Farin, M. 2017. Continuum viscoplastic simulation of a granular column collapse on large slopes: μ(I) rheology and lateral wall effects. Physics of Fluids, **29**(1). doi:10.1063/1.4971320.

Meyrat, G., McArdell, B., Müller, C.R., Munch, J., and Bartelt, P. 2023. Voellmy-type mixture rheologies for dilatant, two-layer debris flow models. Landslides, **20**(11): 2405–2420. doi:10.1007/s10346-023-02092-w.

Midi, G.D.R. 2004. On dense granular flows. European Physical Journal E, **14**(4): 341–365. doi:10.1140/epje/i2003-10153-0.

Mitchell, A., et al. 2022. Variable hydrograph inputs for a numerical debris-flow runout model. Natural Hazards and Earth System Sciences, **22**(5): 1627–1654. doi:10.5194/nhess-22-1627-2022.

Mohamad, A.A. 2011. Lattice Boltzmann method: fundamentals and engineering applications with computer codes, volume 70. Springer, New York. doi:10.1007/978-0-85729-455-5.

Ng, C.W.W., Leonardi, A., Majeed, U., Pirulli, M., and Choi, C.E. 2023. A physical and numerical investigation of flow–barrier interaction for the design of a multiple-barrier system. Journal of Geotechnical and Geoenvironmental Engineering, **149**(1). doi:10.1061/(asce)gt.1943-5606.0002932.

Obrecht, C., Kuznik, F., Tourancheau, B., and Roux, J.J. 2013. Scalable lattice Boltzmann solvers for CUDA GPU clusters. Parallel Computing, **39**(6–7): 259–270. doi:10.1016/j.parco.2013.04.001.

Pasqua, A., Leonardi, A., and Pirulli, M. 2022. Coupling depth-averaged and 3D numerical models for the simulation of granular flows. Computers and Geotechnics, **149**(January): 104879. doi:10.1016/j.compgeo.2022.104879.

Pastor, M., et al. 2015. Depth averaged models for fast landslide propagation: mathematical, rheological and numerical aspects. Archives of Computational Methods in Engineering, **22**(1): 67–104. doi:10.1007/s11831-014-9110-3.

Peng, C., Wu, W., sui Yu, H., and Wang, C. 2015. A SPH approach for large deformation analysis with hypoplastic constitutive model. Acta Geotechnica, **10**(6): 703–717. doi:10.1007/s11440-015-0399-3.

Pirulli, M. 2005. Numerical modelling of landslides runout: a continuum mechanics approach. Ph.D. thesis, Politecnico di Torino.

Pirulli, M. 2010. Morphology and substrate control on the dynamics of flowlike landslides. Journal of Geotechnical and Geoenvironmental Engineering, 376–388. doi:10.1061/ASCEGT.1943-5606.0000221.

Pirulli, M., and Sorbino, G. 2008. Assessing potential debris flow runout: a comparison of two simulation models. Natural Hazards and Earth System Sciences, **8**(4): 961–971. doi:10.5194/nhess-8-961-2008.

Pouliquen, O. 1999. Scaling laws in granular flows down rough inclined planes. Physics of Fluids, **11**(3): 542–548. doi:10.1063/1.1416884.

Pouliquen, O., and Forterre, Y. 2002. Friction law for dense granular flows: application to the motion of a mass down a rough inclined plane. Journal of Fluid Mechanics, **453**(1998): 133–151. doi:10.1017/S0022112001006796.

Pudasaini, S.P., and Mergili, M. 2024. Mechanically controlled landslide deformation. Journal of Geophysical Research: Earth Surface, **129**(5). doi:10.1029/2023JF007466.

Savage, S.B., and Hutter, K. 1989. The motion of a finite mass of granular material down a rough incline. Journal of Fluid Mechanics, **199**(2697): 177–215. doi:10.1017/S0022112089000340.

Takahashi, T. 1981. Debris flow. Annual Review of Fluid Mechanics, 57–77.

Tankeo, M., Richard, P., and Canot, É. 2013. Analytical solution of the μ(I)—rheology for fully developed granular flows in simple configurations. Granular Matter, **15**(6): 881–891. doi:10.1007/s10035-013-0447-3.

van Thang, P., Chopard, B., Lefèvre, L., Ondo, D.A., and Mendes, E. 2010. Study of the 1D lattice Boltzmann shallow water equation and its coupling to build a canal network. Journal of Computer Physics, **229**(19): 7373–7400. doi:10.1016/j.jcp.2010.06.022.

Valette, R., Riber, S., Sardo, L., Castellani, R., Costes, F., Vriend, N., and Hachem, E. 2019. Sensitivity to the rheology and geometry of granular collapses by using the μ(I) rheology. Computers & Fluids, **191**: 1–13. doi:10.1016/j.compfluid.2019.104260.

Winter, M.G., Shearer, B., Palmer, D., Peeling, D., Harmer, C., and Sharpe, J. 2016. The economic impact of landslides and floods on the road network. Procedia Engineer, **143**(Ictg): 1425–1434. doi:10.1016/j.proeng.2016.06.168.

Wu, Y., Wang, D., Li, P., and Niu, Z. 2022. Experimental investigation of dry granular flows down an inclined channel against a wall-like obstacle of limited width. Acta Geotechnica, **2**. doi:10.1007/s11440-022-01714-2.

Yang, G.C., Huang, Y.J., Lu, Y., Kwok, C.Y., Sobral, Y.D., and Yao, Q.H. 2023. Frictional boundary condition for lattice Boltzmann modelling of dense granular flows. Journal of Fluid Mechanics, **973**: 1–32. doi:10.1017/jfm.2023.782.

Yuan, W.H., Wang, B., Zhang, W., Jiang, Q., and Feng, X.T. 2019. Development of an explicit smoothed particle finite element method for geotechnical applications. Computers and Geotechnics, **106**(April 2018): 42–51. doi:10.1016/j.compgeo.2018.10.010.

Zhang, J. 2011. Lattice Boltzmann method for microfluidics: models and applications. Microfluidics and Nanofluidics, **10**(1): 1–28. doi:10.1007/s10404-010-0624-1.

Zhao, L., He, J.W., Yu, Z.X., Liu, Y.P., Zhou, Z.H., and Chan, S.L. 2020. Coupled numerical simulation of a flexible barrier impacted by debris flow with boulders in front. Landslides, **17**(12): 2723–2736. doi:10.1007/s10346-020-01463-x.

Zou, Q., and He, X. 1997. On pressure and velocity boundary conditions for the lattice Boltzmann BGK model. Physics of Fluids, **9**(6): 1591–1598. doi:10.1063/1.869307.